Journal of Fluids and Structures 98 (2020) 103117

Contents lists available at ScienceDirect

Journal of Fluids and Structures

journal homepage: www.elsevier.com/locate/jfs

An energy stable one-field monolithic arbitrary Lagrangian–Eulerian formulation for fluid–structure interaction

Yongxing Wang [a,*], Peter K. Jimack [b], Mark A. Walkley [b], Olivier Pironneau [c]

[a] School of Mechanical Engineering, University of Leeds, Leeds, LS2 9JT, UK
[b] School of Computing, University of Leeds, Leeds, LS2 9JT, UK
[c] Laboratoire Jacques-Louis Lions, Sorbonne Universités, Paris, France

ARTICLE INFO

Article history:
Received 3 March 2020
Received in revised form 23 July 2020
Accepted 23 July 2020
Available online 30 July 2020

Keywords:
Fluid structure interaction
Finite element
One field
Monolithic scheme
Arbitrary Lagrangian–Eulerian
Energy stable

ABSTRACT

In this article we present a one-field monolithic finite element method in the Arbitrary Lagrangian–Eulerian (ALE) formulation for Fluid–Structure Interaction (FSI) problems. The method only solves for one velocity field in the whole FSI domain, and it solves in a monolithic manner so that the fluid solid interface conditions are satisfied automatically. We prove that the proposed scheme is unconditionally stable, through energy analysis, by utilising a conservative formulation and an exact quadrature rule. We implement the algorithm using both **F**-scheme and **d**-scheme, and demonstrate that the former has the same formulation in two and three dimensions. Finally several numerical examples are presented to validate this methodology, including combination with remesh techniques to handle the case of very large solid displacement.

1. Introduction

Numerical methods for Fluid–Structure Interaction (FSI) have been widely studied during the past decades, and a variety of methodologies have been developed in order to address different aspects of the FSI problem. However stability analyses of the existing numerical methods are rare especially when large solid deformation is involved. This paper is dedicated to developing a one-field monolithic FSI method in the Arbitrary Lagrangian–Eulerian (ALE) framework, and establishing its stability analysis over time.

Monolithic methods have been regarded as the most robust FSI algorithms in the literature (Bendiksen et al., 1991; Blom, 1998; Heil, 2004; Heil et al., 2008; Muddle et al., 2012; Hecht and Pironneau, 2017; Wang et al., 2017, 2019; Hübner et al., 2004), which solve for the fluid and solid variables simultaneously in one equation system. Among these methodologies for FSI problems, the one-field approaches (Bendiksen, 1991; Hecht and Pironneau, 2017; Wang et al., 2017; Hübner et al., 2004) express the solid equation in terms of velocity, thus only solve for one velocity in the whole FSI domain. In this case the whole system can be solved similarly to a modified fluid problem, and the coupling conditions at fluid and solid interface are automatically satisfied.

The stability analysis when using the ALE framework is challenging, even for the pure fluid problem, due to the arbitrary moving frame (Nobile and Formaggia, 1999; Formaggia and Nobile, 2004; Bonito et al., 2013). Boffi and Gastaldi (2016), Boffi et al. (2015) present an energy stable Fictitious Domain Method with Distributed Lagrangian Multiplier (FDM/DLM),

* Corresponding author.
E-mail address: scsywan@leeds.ac.uk (Y. Wang).

https://doi.org/10.1016/j.jfluidstructs.2020.103117
0889-9746/

and Hecht and Pironneau (2017) and Pironneau (2016b) present an energy stable Eulerian formulation by remeshing. There is also some analysis on the existence and stability of solutions of different FSI formulations, such as Du et al. (2003), Lequeurre (2011), Grandmont and Maday (2000), Nobile and Vergara (2008). In a previous study (Wang et al., 2019) we analysed the energy stability for a one-field FDM method. In this article we extend this one-field idea to the ALE formulation, and the stability result is achieved by expressing the fluid and solid equations in a conservative formulation. In this sense, the formulation is similar to the one introduced in Hecht and Pironneau (2017). However it differs from Hecht and Pironneau (2017) in the following perspectives: (1) we formulate the solid in the reference domain and analyse the FSI problem in an ALE frame of reference, in which case the formulation and analysis are exactly the same for two and three dimensional cases, whereas Hecht and Pironneau (2017) formulates and analyses everything in the current domain, for which the three dimensional case is significantly more complicated (Chiang et al., 2017); (2) we update the solid deformation tensor (the **F**-scheme) while Hecht and Pironneau (2017) updates the solid displacement (the **d**-scheme); (3) we implement the scheme by solving an additional solid-like equation at each time step in order to move the mesh, whilst Hecht and Pironneau (2017) implements their scheme by remeshing which is expensive in the three dimensional case.

The paper is organised as follows. In Section 2 the control equations for the FSI problem are introduced in an ALE framework. In Section 3 the finite element weak formulation is introduced, followed by spatial and time discretisations in Section 4. The main results of energy stability are presented in Section 5. Implementation details are considered in Section 6 and numerical examples are given in Section 7, with some conclusions in Section 8.

2. The arbitrary Lagrangian–Eulerian description for the FSI problem

Let $\Omega_t^f \subset \mathbb{R}^d$ and $\Omega_t^s \subset \mathbb{R}^d$ be the fluid and solid domain respectively (which are time dependent regions), $\Gamma_t = \overline{\Omega}_t^f \cap \overline{\Omega}_t^s$ is the moving interface between the fluid and solid, and $\Omega_t = \overline{\Omega}_t^f \cup \overline{\Omega}_t^s$ has an outer boundary $\partial\Omega_t$, which can be fixed or moving as shown in Fig. 1. We use the superscripts f and s to denote the fluid and solid variables respectively in the above and throughout this article. The Eulerian description is convenient when we observe a fluid from a fixed frame, while the Lagrangian description is convenient when we observe a solid from a frame moving with it. An ALE frame of reference can be adopted when a fluid and solid share an interface and interact with each other as shown in Fig. 1, in which case the frame moves arbitrarily from a reference configuration Ω_{t_0}, chosen to be the same as the initial configuration at t_0, to a current configuration Ω_t. Let us define a family of mappings $\mathcal{A}_t$:

$$\mathcal{A}_t : \Omega_{t_0} \subset \mathbb{R}^d \to \Omega_t \subset \mathbb{R}^d, \tag{1}$$

with $d = 2, 3$ being the dimensions. We assume that $\mathcal{A}_t \in C^0\left(\overline{\Omega}_{t_0}\right)^d$ is one-to-one and invertible with continuous inverse $\mathcal{A}_t^{-1} \in C^0\left(\overline{\Omega}_t\right)^d$. Hence a point $\hat{\mathbf{x}} \in \Omega_{t_0}$ has a unique image $\mathbf{x} \in \Omega_t$ at time t, i.e.

$$\mathbf{x} = \mathcal{A}\left(\hat{\mathbf{x}}, t\right) = \mathcal{A}_t\left(\hat{\mathbf{x}}\right), \tag{2}$$

and a point $\mathbf{x} \in \Omega_t$ at time t has a unique inverse image $\hat{\mathbf{x}} \in \Omega_{t_0}$

$$\hat{\mathbf{x}} = \hat{\mathcal{A}}\left(\mathbf{x}, t\right) = \mathcal{A}_t^{-1}\left(\mathbf{x}\right). \tag{3}$$

We call $\mathbf{x} \in \Omega_t$ the Eulerian coordinate, and call its inverse image $\hat{\mathbf{x}}$, via the above mapping $\mathcal{A}_t^{-1}$, the ALE coordinate. We assume that $\mathcal{A}\left(\hat{\mathbf{x}}, t\right)$ is differentiable with respect to t for all $\hat{\mathbf{x}} \in \Omega_{t_0}$, and define the velocity of the ALE frame as

$$\mathbf{w}\left(\hat{\mathbf{x}}, t\right) = \frac{\partial \mathcal{A}}{\partial t}\left(\hat{\mathbf{x}}, t\right). \tag{4}$$

Given an Eulerian coordinate $\mathbf{x} \in \Omega_t$, its corresponding ALE coordinate $\hat{\mathbf{x}}_1 \in \Omega_{t_0}$ should be distinguished from its material (or Lagrangian) coordinate $\hat{\mathbf{x}}_2 \in \Omega_{t_0}$ as shown in Fig. 1. In fact $\hat{\mathbf{x}}_2 \in \Omega_{t_0}$ (not necessarily the same as $\hat{\mathbf{x}}_1$) maps to $\mathbf{x} \in \Omega_t$ via the Lagrangian mapping, i.e., the trajectory of a material particle at $\hat{\mathbf{x}}_2$:

$$\mathcal{F}_t : \hat{\mathbf{x}} \mapsto \mathbf{x} = \mathcal{F}\left(\hat{\mathbf{x}}, t\right), \tag{5}$$

and the velocity of the material particle at $\hat{\mathbf{x}} \in \Omega_{t_0}$ is defined by

$$\mathbf{u}\left(\hat{\mathbf{x}}, t\right) = \frac{\partial \mathcal{F}}{\partial t}. \tag{6}$$

Remark 1. Although the Lagrangian configuration and the ALE configuration are not generally the same, both are chosen to have the initial configuration Ω_{t_0} in this article. We shall also construct the ALE mapping such that $\mathcal{A}_t\left(\Omega_{t_0}\right)$ coincides with $\mathcal{F}_t\left(\Omega_{t_0}\right)$ at all boundaries including the fluid–solid interface: $\mathcal{A}_t\left(\partial\Omega_{t_0}\right) = \mathcal{F}_t\left(\partial\Omega_{t_0}\right)$ and $\mathcal{A}_t\left(\Gamma_t\right) = \mathcal{F}_t\left(\Gamma_t\right)$.

Remark 2. The ALE mapping is the mapping that is actually used to move the domain in this article, and the purpose of introducing the Lagrangian mapping is to discuss its related variables, such as particle velocity **u** and solid deformation tensor **F**, which will be defined in the following context.

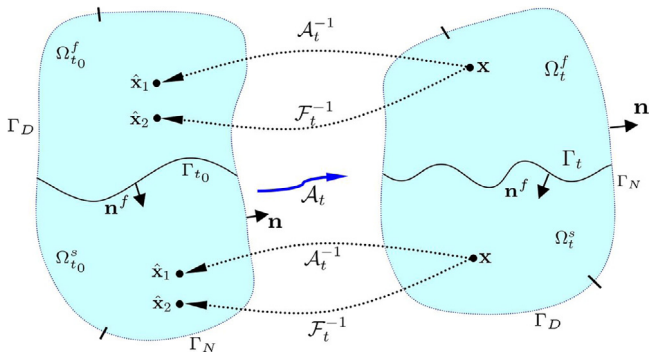

Fig. 1. ALE mapping from Ω_{t_0} to Ω_t. Also shows the comparison between ALE mapping and Lagrangian mapping with Eulerian coordinate $\mathbf{x}$, ALE coordinate $\hat{\mathbf{x}}_1$ and material (Lagrangian) coordinate $\hat{\mathbf{x}}_2$. $\Gamma_t = \overline{\Omega}_t^f \cap \overline{\Omega}_t^s$ and $\Omega_t = \overline{\Omega}_t^f \cup \overline{\Omega}_t^s$, $\partial\Omega_t = \Gamma_D \cup \Gamma_N$.

Formulated in the current configuration, the conservation of momentum takes the same form in the fluid and solid domain Ω:

$$\rho \frac{d\mathbf{u}(\mathbf{x}, t)}{dt} = \operatorname{div}(\boldsymbol{\sigma}) + \rho \mathbf{g}, \tag{7}$$

with ρ, $\mathbf{g}$, $\mathbf{u}$ and $\boldsymbol{\sigma}$ being the density, gravity acceleration, velocity and Cauchy stress tensor respectively. Here we use the notation $\rho = \begin{cases} \rho^f & in \quad \Omega_t^f \\ \rho^s & in \quad \Omega_t^s \end{cases}$, with the superscript f and s denote fluid and solid respectively, and similar notations are also applied to $\mathbf{u}$ and $\boldsymbol{\sigma}$. In the above, $\frac{d(\cdot)}{dt}$ is the total derivative computed along the trajectory of a material particle at $\mathbf{x}$, i.e. via the Lagrangian mapping:

$$\frac{d\mathbf{u}(\mathbf{x}, t)}{dt} = \frac{d\mathbf{u}\left(\mathcal{F}_t\left(\hat{\mathbf{x}}\right), t\right)}{dt} = \left.\frac{\partial \mathbf{u}}{\partial t}\right|_{\mathbf{x}=\mathcal{F}(\hat{\mathbf{x}}, t)} + (\mathbf{u} \cdot \nabla)\mathbf{u}. \tag{8}$$

Replacing the above partial time derivative by the total derivative of

$$\frac{d\mathbf{u}\left(\mathcal{A}_t\left(\hat{\mathbf{x}}\right), t\right)}{dt} = \left.\frac{\partial \mathbf{u}}{\partial t}\right|_{\mathbf{x}=\mathcal{A}(\hat{\mathbf{x}}, t)} + (\mathbf{w} \cdot \nabla)\mathbf{u} \tag{9}$$

leads to the ALE formulation of (7)

$$\rho \frac{d\mathbf{u}\left(\mathcal{A}_t\left(\hat{\mathbf{x}}\right), t\right)}{dt} + \rho((\mathbf{u} - \mathbf{w}) \cdot \nabla)\mathbf{u} = \operatorname{div}(\boldsymbol{\sigma}) + \rho \mathbf{g} \quad \text{in} \quad \Omega. \tag{10}$$

We consider here both an incompressible fluid and incompressible solid:

$$\boldsymbol{\sigma} = \boldsymbol{\tau} - p\mathbf{I}, \tag{11}$$

with $\boldsymbol{\tau}$ being the deviatoric part of the stress tensor. For a Newtonian fluid in Ω_t^f,

$$\boldsymbol{\tau} = \boldsymbol{\tau}^f = \mu^f \mathrm{D}\mathbf{u} = \mu^f \left(\nabla \mathbf{u} + \nabla^T \mathbf{u}\right), \tag{12}$$

and for a hyperelastic solid (Belytschko et al., 2013) in Ω_t^s,

$$\boldsymbol{\tau} = \boldsymbol{\tau}^s = J_{\mathcal{F}_t}^{-1} \frac{\partial \Psi(\mathbf{F})}{\partial \mathbf{F}} \mathbf{F}^T, \tag{13}$$

with

$$\mathbf{F} = \frac{\partial \mathcal{F}\left(\hat{\mathbf{x}}, t\right)}{\partial \hat{\mathbf{x}}} \tag{14}$$

being the deformation tensor of the solid, $J_{\mathcal{F}_t}$ being the determinant of $\mathbf{F}$, and $\Psi(\mathbf{F})$ being the energy function of the hyperelastic solid material. Combining with the continuity equation

$$\nabla \cdot \mathbf{u} = 0 \quad \text{in} \quad \Omega_t, \tag{15}$$

the FSI system is completed with continuity of the velocity and normal stress conditions on the interface Γ_t:

$$\mathbf{u}^f = \mathbf{u}^s, \quad \boldsymbol{\sigma}^f \mathbf{n}^f = \boldsymbol{\sigma}^s \mathbf{n}^f, \tag{16}$$

and (for simplicity of this exposition) homogeneous Dirichlet and Neumann boundaries on Γ_D and Γ_N respectively:

$$\mathbf{u} = 0, \quad \boldsymbol{\sigma}\mathbf{n} = 0, \tag{17}$$

with $\Gamma_D \cup \Gamma_N = \partial\Omega_t$ as shown in Fig. 1.

3. Finite element weak formulation

Let $L^2(\omega)$ be the square integrable functions in domain ω, endowed with norm $\|u\|_{0,\omega}^2 = \int_\omega |u|^2$. Let $H^1(\omega) = \left\{u : u \in L^2(\omega), \nabla u \in L^2(\omega)^d\right\}$ with the norm denoted by $\|u\|_{1,\omega}^2 = \|u\|_{0,\omega}^2 + \|\nabla u\|_{0,\omega}^2$. We also denote by $H_0^1(\omega)$ the subspace of $H^1(\omega)$ whose functions have zero value on the Dirichlet boundary of ω.

According to Eq. (2) we construct Ω_t from Ω_{t_0}, so a function $v \in H_0^1(\Omega_t)$ is one-to-one corresponding to a function $\hat{v} \in H_0^1(\Omega_{t_0})$ via

$$v \circ \mathcal{A}_t = \hat{v}. \tag{18}$$

Choosing a test function $\mathbf{v}(\mathbf{x}) = \mathbf{v} \circ \mathcal{A}_t\left(\hat{\mathbf{x}}\right) = \hat{\mathbf{v}}\left(\hat{\mathbf{x}}\right)$, the weak formulation may be obtained by multiplying $\mathbf{v}$ on both sides of Eq. (10), and integrating the stress term by parts in domain Ω_t^f and Ω_t^s separately:

$$\begin{aligned} &\rho^f \int_{\Omega_t^f} \frac{d\mathbf{u}\left(\mathcal{A}_t\left(\hat{\mathbf{x}}\right), t\right)}{dt} \cdot \mathbf{v} + \rho^f \int_{\Omega_t^f} \left((\mathbf{u} - \mathbf{w}) \cdot \nabla\right) \mathbf{u} \cdot \mathbf{v} \\ &+ \frac{\mu^f}{2} \int_{\Omega_t^f} \mathrm{D}\mathbf{u} : \mathrm{D}\mathbf{v} - \int_{\Omega_t^f} p\nabla \cdot \mathbf{v} = \int_{\partial\Omega_t^f} \boldsymbol{\sigma}^f \mathbf{n}^f \cdot \mathbf{v} + \rho^f \int_{\Omega_t^f} \mathbf{g} \cdot \mathbf{v}. \end{aligned} \tag{19}$$

$$\begin{aligned} &\rho^s \int_{\Omega_t^f} \frac{d\mathbf{u}\left(\mathcal{A}_t\left(\hat{\mathbf{x}}\right), t\right)}{dt} \cdot \mathbf{v} + \rho^s \int_{\Omega_t^f} \left((\mathbf{u} - \mathbf{w}) \cdot \nabla\right) \mathbf{u} \cdot \mathbf{v} \\ &+ \int_{\Omega_{t_0}^s} \frac{\partial \Psi}{\partial \mathbf{F}} : \nabla_{\hat{\mathbf{x}}} \mathbf{v} - \int_{\Omega_t^s} p\nabla \cdot \mathbf{v} = \int_{\partial\Omega_t^s} \boldsymbol{\sigma}^s \left(-\mathbf{n}^f\right) \cdot \mathbf{v} + \rho^s \int_{\Omega_t^s} \mathbf{g} \cdot \mathbf{v}. \end{aligned} \tag{20}$$

We used $\frac{\partial \Psi}{\partial \mathbf{F}} \mathbf{F}^T : \nabla \mathbf{v} = \frac{\partial \Psi}{\partial \mathbf{F}} : \nabla \mathbf{v}\mathbf{F} = \frac{\partial \Psi}{\partial \mathbf{F}} : \nabla_{\hat{\mathbf{x}}} \mathbf{v}$ in the above deduction. Using the interface and boundary conditions (16) and (17), we have the following equation by adding up (19) and (20).

$$\begin{aligned} &\rho \int_{\Omega_t} \frac{d\mathbf{u}\left(\mathcal{A}_t\left(\hat{\mathbf{x}}\right), t\right)}{dt} \cdot \mathbf{v} + \rho \int_{\Omega_t} \left((\mathbf{u} - \mathbf{w}) \cdot \nabla\right) \mathbf{u} \cdot \mathbf{v} \\ &+ \frac{\mu^f}{2} \int_{\Omega_t^f} \mathrm{D}\mathbf{u} : \mathrm{D}\mathbf{v} - \int_{\Omega_t} p\nabla \cdot \mathbf{v} + \int_{\Omega_{t_0}^s} \frac{\partial \Psi}{\partial \mathbf{F}} : \nabla_{\hat{\mathbf{x}}} \mathbf{v} = \rho \int_{\Omega_t} \mathbf{g} \cdot \mathbf{v}. \end{aligned} \tag{21}$$

Using Jacobi's formula (Magnus and Neudecker, 2019), we have

$$\begin{aligned} \frac{\partial J_{\mathcal{A}_t}}{\partial t} &= trace\left(J_{\mathcal{A}_t} \mathbf{A}^{-1} \frac{\partial \mathbf{A}}{\partial t}\right) \\ &= trace\left(J_{\mathcal{A}_t} \mathbf{A}^{-1} \nabla_{\hat{\mathbf{x}}} \frac{\partial \mathcal{A}_t}{\partial t}\right) \\ &= J_{\mathcal{A}_t} \nabla \cdot \frac{\partial \mathcal{A}_t}{\partial t} = J_{\mathcal{A}_t} \nabla \cdot \mathbf{w}, \end{aligned} \tag{22}$$

with $\mathbf{A} = \frac{\partial \mathcal{A}(\hat{\mathbf{x}}, t)}{\partial \hat{\mathbf{x}}} = \nabla_{\hat{\mathbf{x}}} \mathcal{A}_t$. Then we can take the time derivative outside the moving domain (conservative formulation Nobile and Formaggia, 1999),

$$\begin{aligned} &\frac{d}{dt} \int_{\Omega_t} \mathbf{u}(\mathbf{x}, t) \cdot \mathbf{v}(\mathbf{x}) = \frac{d}{dt} \int_{\Omega_{t_0}} J_{\mathcal{A}_t} \mathbf{u}\left(\mathcal{A}_t\left(\hat{\mathbf{x}}\right), t\right) \cdot \hat{\mathbf{v}}\left(\hat{\mathbf{x}}\right) \\ &= \int_{\Omega_t} \frac{d\mathbf{u}(\mathbf{x}, t)}{dt} \cdot \mathbf{v}(\mathbf{x}) + \int_{\Omega_t} (\nabla \cdot \mathbf{w}) \mathbf{u}(\mathbf{x}, t) \cdot \mathbf{v}(\mathbf{x}). \end{aligned} \tag{23}$$

Substituting (23) into (21), using

$$\mathrm{div}(\mathbf{w} \otimes \mathbf{u}) = (\mathbf{w} \cdot \nabla)\mathbf{u} + (\nabla \cdot \mathbf{w})\mathbf{u}, \tag{24}$$

and combining the weak form of continuity equation (15), leads to the weak formulation of the FSI problem:

Problem 1. Given Ω_{t_0}, Γ_{t_0}, $\mathbf{u}(\hat{\mathbf{x}}, t_0)$ and an ALE mapping $\mathcal{A}_t$ (consequently given $\mathbf{w}$ by (4)), $\forall \hat{\mathbf{x}} \in \Omega_{t_0}$: $\forall t \in (0, T]$ find $\mathbf{u}(\mathbf{x}, t) = \mathbf{u}(\mathcal{A}_t(\hat{\mathbf{x}}), t) \in H_0^1(\Omega_t)^d$ and $p(\mathbf{x}, t) = p(\mathcal{A}_t(\hat{\mathbf{x}}), t) \in L^2(\Omega_t)$, such that $\forall \mathbf{v}(\mathbf{x}) = \mathbf{v}(\mathcal{A}_t(\hat{\mathbf{x}}))$, $\mathbf{v} \in H_0^1(\Omega_t)^d$ and $\forall q(\mathbf{x}) = q(\mathcal{A}_t(\hat{\mathbf{x}}))$, $q \in L^2(\Omega_t)$, the following equations hold:

$$\begin{aligned} &\rho \frac{d}{dt} \int_{\Omega_t} \mathbf{u}\left(\mathcal{A}_t(\hat{\mathbf{x}}), t\right) \cdot \mathbf{v} + \rho \int_{\Omega_t} (\mathbf{u} \cdot \nabla)\, \mathbf{u} \cdot \mathbf{v} + \rho \int_{\Omega_t} (\mathbf{w} \otimes \mathbf{u}) : \nabla \mathbf{v} \\ &+ \frac{\mu^f}{2} \int_{\Omega_t^f} \mathrm{D}\mathbf{u} : \mathrm{D}\mathbf{v} - \int_{\Omega_t} p \nabla \cdot \mathbf{v} + \int_{\Omega_{t_0}^s} \frac{\partial \Psi}{\partial \mathbf{F}}(\mathbf{F}) : \nabla_{\hat{\mathbf{x}}} \mathbf{v} = \rho \int_{\Omega_t} \mathbf{g} \cdot \mathbf{v}, \end{aligned} \tag{25}$$

$$- \int_{\Omega_t} q \nabla \cdot \mathbf{u} = 0, \tag{26}$$

and

$$\mathcal{A}_t\left(\partial \Omega_{t_0}\right) = \mathcal{F}_t\left(\partial \Omega_{t_0}\right), \quad \mathcal{A}_t\left(\Gamma_t\right) = \mathcal{F}_t\left(\Gamma_t\right), \tag{27}$$

with Γ_{t_0} and $\partial \Omega_{t_0}$ being the initial interface and outer boundary respectively, as shown in Fig. 1, and $\mathcal{F}_t$ being the Lagrangian mapping as defined in (5).

4. Discretisation in space and time

Define a stable finite element space, such as the Taylor–Hood elements, for the velocity–pressure pair $(\mathbf{u}, p)$ in Ω_{t_0}:

$$V^h\left(\Omega_{t_0}\right) = span\left\{\hat{\varphi}_1, \ldots, \hat{\varphi}_{N^u}\right\} \subset H_0^1\left(\Omega_{t_0}\right)$$

and

$$L^h(\Omega_{t_0}) = span\left\{\hat{\phi}_1, \ldots, \hat{\phi}_{N^p}\right\} \subset L^2\left(\Omega_{t_0}\right),$$

with N^u and N^p being the number of nodal variables for each velocity component and pressure respectively. Then

$$V^h(\Omega_t) = \left\{\varphi_h : \varphi_h = \hat{\varphi}_h \circ \mathcal{A}_t^{-1}, \hat{\varphi}_h \in V^h\left(\Omega_{t_0}\right)\right\},$$

and

$$L^h(\Omega_t) = \left\{\phi_h : \phi_h = \hat{\phi}_h \circ \mathcal{A}_t^{-1}, \hat{\phi}_h \in L^h\left(\Omega_{t_0}\right)\right\}.$$

Using the backward Euler scheme, Eqs. (25) and (26) can be discretised respectively as follows:

$$\begin{aligned} &\frac{\rho}{\delta t} \int_{\Omega_{t_{n+1}}} \mathbf{u}_{n+1}^h \cdot \mathbf{v} - \frac{\rho}{\delta t} \int_{\Omega_{t_n}} \mathbf{u}_n^h \cdot \mathbf{v} + \rho \int_{\Omega_{t_{n+1}}} \left(\mathbf{u}_{n+1}^h \cdot \nabla\right) \mathbf{u}_{n+1}^h \cdot \mathbf{v} \\ &+ \rho \mathcal{I}(\xi(\tau)) + \frac{\mu^f}{2} \int_{\Omega_{t_{n+1}}^f} \mathrm{D}\mathbf{u}_{n+1}^h : \mathrm{D}\mathbf{v} - \int_{\Omega_{t_{n+1}}} p_{n+1}^h \nabla \cdot \mathbf{v} \\ &+ \int_{\Omega_{t_0}^s} \frac{\partial \Psi}{\partial \mathbf{F}}(\mathbf{F}_{n+1}) : \nabla_{\hat{\mathbf{x}}} \mathbf{v} = \int_{\Omega_{t_{n+1}}} \rho \mathbf{g} \cdot \mathbf{v}, \end{aligned} \tag{28}$$

and

$$- \int_{\Omega_{t_{n+1}}} q \nabla \cdot \mathbf{u}_{n+1}^h = 0. \tag{29}$$

In the above

$$\xi(\tau) = \int_{\Omega_\tau} \left(\mathbf{w}(\tau) \otimes \mathbf{u}_{n+1}^h\right) : \nabla \mathbf{v}, \tag{30}$$

and $\delta t \mathcal{I}(\xi)$ is a quadrature formula used to compute $\int_{t_n}^{t_{n+1}} \xi(\tau)$. In order to have an unconditionally stable scheme, which will be proved in Section 5, the mid-point integration is adopted for this term, i.e.:

$$\mathcal{I}(\xi) = \xi\left(t_{n+1/2}\right) \tag{31}$$

in the two dimensional case, and the Simpson formula is adopted in the three dimensional case:

$$\mathcal{I}(\xi) = \frac{2}{3}\xi\left(t_{n+1/2}\right) + \frac{1}{6}\xi\left(t_n\right) + \frac{1}{6}\xi\left(t_{n+1}\right). \tag{32}$$

Notice that the Simpson formula can also be adopted in the two dimensional case, but the mid-point rule is simpler (and still of the same order as the temporal discretisation). Due to the definition of the deformation tensor $\mathbf{F}$ (14) and ALE velocity $\mathbf{w}$ (4), we have

$$\frac{\mathbf{F}_{n+1}-\mathbf{F}_n}{\delta t}=\frac{\mathbf{F}_{n+1}\circ\mathcal{F}_{t_{n+1}}\left(\hat{\mathbf{x}}\right)-\mathbf{F}_n\circ\mathcal{F}_{t_n}\left(\hat{\mathbf{x}}\right)}{\delta t}\approx\nabla_{\hat{\mathbf{x}}}\mathbf{u}_{n+1}, \tag{33}$$

and

$$\frac{\mathbf{x}_{n+1}-\mathbf{x}_n}{\delta t}=\frac{\mathcal{A}_{t_{n+1}}\left(\hat{\mathbf{x}}\right)-\mathcal{A}_{t_n}\left(\hat{\mathbf{x}}\right)}{\delta t}\approx\mathbf{w}_{n+1}. \tag{34}$$

Therefore $\mathbf{F}_{n+1}$ and $\Omega_{t_{n+1}}$ in (28) can be updated as follows:

$$\mathbf{F}_{n+1}=\mathbf{F}_n+\delta t\nabla_{\hat{\mathbf{x}}}\mathbf{u}_{n+1}, \tag{35}$$

and

$$\Omega_{t_{n+1}}=\mathcal{A}_{t_{n+1}}\left(\Omega_{t_0}\right)=\left\{\mathbf{x}:\mathbf{x}=\mathbf{x}_n+\delta t\mathbf{w}_{n+1},\mathbf{x}_n\in\mathcal{A}_{t_n}\left(\Omega_{t_0}\right)\right\}. \tag{36}$$

Up to now we have not stated how to construct $\mathbf{w}$ (or $\mathcal{A}_t$), because very often we only need to construct the ALE mapping $\mathcal{A}_t$ at a discrete time level, that is to say computing $\mathcal{A}_{t_{n+1}}$ for $n=0,1,\ldots$ at each time step. This will be explained in the rest of this section.

We solve the following static linear elastic equation in $\Omega_{t_{n+1}}$ in order to compute $\mathbf{w}_{n+1}$, and take $\mathbf{w}(t)=\mathbf{w}_{n+1}$ for $t\in(t_n,t_{n+1}]$. Given the following boundary data:

$$\mathbf{w}_{n+1}\cdot\mathbf{n}=0,\quad \mathbf{n}\cdot\mathrm{D}\mathbf{w}_{n+1}\cdot\mathbf{t}=0\qquad\text{on}\quad\partial\Omega_{t_{n+1}}, \tag{37}$$

and

$$\mathbf{w}_{n+1}=\mathbf{u}^h_{n+1}\qquad\text{on}\quad\Gamma_{t_{n+1}}, \tag{38}$$

find $\mathbf{w}_{n+1}\in V^h(\Omega_{t_{n+1}})^d$ such that $\forall\mathbf{z}\in V^h(\Omega_{t_{n+1}})^d$, the following equation holds:

$$\frac{\mu}{2}\int_{\Omega_{t_{n+1}}}\mathrm{D}\mathbf{w}_{n+1}:\mathrm{D}\mathbf{z}+\lambda\int_{\Omega_{t_{n+1}}}\left(\nabla\cdot\mathbf{w}_{n+1}\right)\left(\nabla\cdot\mathbf{z}\right)=0, \tag{39}$$

with μ and λ being the Lamé constants used here as pseudo-solid parameters, which may be different from the solid parameters (Richter and Wick, 2010). It is well known that the above elliptic problem (37) to (39) has a unique solution $\mathbf{w}\in V^h\left(\Omega_{t_{n+1}}\right)$ (Brenner and Scott, 2007) (notice that $\mathbf{n}\cdot\mathrm{D}\mathbf{w}_{n+1}\cdot\mathbf{t}=0$ on $\partial\Omega_{t_{n+1}}$ should be enforced for the corresponding PDE equation of (39), with $\mathbf{t}$ being the tangential direction of $\partial\Omega_{t_{n+1}}$). As a result, we are able to construct a mapping for $t\in(t_n,t_{n+1}]$,

$$\mathcal{A}_{t_n,t}:\Omega_{t_n}\to\Omega_t,\quad \mathcal{A}_{t_n,t}\left(\mathbf{x}_n\right)=\mathbf{x}_n+(t-t_n)\mathbf{w}_{n+1}, \tag{40}$$

and further

$$\mathcal{A}_t=\mathcal{A}^{-1}_{t_0,t_1}\circ\mathcal{A}^{-1}_{t_1,t_2}\cdots\circ\mathcal{A}^{-1}_{t_n,t}. \tag{41}$$

From the computational point of view, knowing the ALE velocity $\mathbf{w}_{n+1}$ at the discrete level is sufficient.

Putting all the above together, the discrete ALE-FSI problem reads:

Problem 2. Given $\mathcal{A}_{t_n}$ and $\mathbf{u}^h_n=\mathbf{u}(\mathcal{A}_{t_n}\left(\hat{\mathbf{x}}\right),t_n)$, $\forall\hat{\mathbf{x}}\in\Omega_{t_0}$ find $\mathbf{u}^h_{n+1}=\mathbf{u}(\mathcal{A}_{t_{n+1}}\left(\hat{\mathbf{x}}\right),t_{n+1})\in V^h(\Omega_{t_{n+1}})^d$, $p^h_{n+1}=p(\mathcal{A}_{t_{n+1}}\left(\hat{\mathbf{x}}\right),t_{n+1})\in L^h(\Omega_{t_{n+1}})$, and $\mathbf{w}_{n+1}\in V^h(\Omega_{t_{n+1}})^d$ (consequently an ALE mapping $\mathcal{A}_{t_{n+1}}$ by (41)), such that $\forall\mathbf{v}(\mathbf{x})=\mathbf{v}(\mathcal{A}_{t_{n+1}}\left(\hat{\mathbf{x}}\right))$, $\mathbf{v}\in V^h(\Omega_{t_{n+1}})^d$, $\forall q(\mathbf{x})=q(\mathcal{A}_{t_{n+1}}\left(\hat{\mathbf{x}}\right))$, $q\in L^h(\Omega_{t_{n+1}})$ and $\forall\mathbf{z}\in V^h(\Omega_{t_{n+1}})^d$, the following equation system holds:

$$\begin{aligned}
&\frac{\rho}{\delta t}\int_{\Omega_{t_{n+1}}}\mathbf{u}^h_{n+1}\cdot\mathbf{v}-\frac{\rho}{\delta t}\int_{\Omega_{t_n}}\mathbf{u}^h_n\cdot\mathbf{v}+\rho\int_{\Omega_{t_{n+1}}}\left(\mathbf{u}^h_{n+1}\cdot\nabla\right)\mathbf{u}^h_{n+1}\cdot\mathbf{v}\\
&+\rho\mathcal{I}\left(\xi(\tau)\right)+\frac{\mu^f}{2}\int_{\Omega^f_{t_{n+1}}}\mathrm{D}\mathbf{u}^h_{n+1}:\mathrm{D}\mathbf{v}-\int_{\Omega_{t_{n+1}}}p^h_{n+1}\nabla\cdot\mathbf{v}\\
&-\int_{\Omega_{t_{n+1}}}q\nabla\cdot\mathbf{u}^h_{n+1}+\int_{\Omega^s_{t_0}}\frac{\partial\Psi}{\partial\mathbf{F}}\left(\mathbf{F}_{n+1}\right):\nabla_{\hat{\mathbf{x}}}\mathbf{v}\\
&+\frac{\mu}{2}\int_{\Omega_{t_{n+1}}}\mathrm{D}\mathbf{w}_{n+1}:\mathrm{D}\mathbf{z}+\lambda\int_{\Omega_{t_{n+1}}}\left(\nabla\cdot\mathbf{w}_{n+1}\right)\left(\nabla\cdot\mathbf{z}\right)=\int_{\Omega_{t_{n+1}}}\rho\mathbf{g}\cdot\mathbf{v}.
\end{aligned} \tag{42}$$

with quadrature formula (31) in 2D or (32) in 3D, updating $\mathbf{F}_{n+1}$ by (35) and updating $\Omega_{t_{n+1}}$ by (36). In addition, the above FSI system equations are completed with the Dirichlet and Neumann boundary conditions (17) for the momentum and continuity equations (28) and (29), and with the boundary conditions (37) and (38) for the mesh equation (39).

Problem 2 is a highly non-linear system, so we solve it iteratively as described in the following Algorithm 1.

Algorithm 1 Solve Problem 2 for $\mathcal{A}_{t_{n+1}}$ (or $\mathbf{w}^h_{n+1}$), $\mathbf{u}^h_{n+1}$ and p^h_{n+1}

Require: $\Omega_{t_n} = \mathcal{A}_{t_n}\left(\Omega_{t_0}\right)$, $\mathbf{u}^h_n$ and a tolerance *tol*
Ensure: $\Omega_{t^0_{n+1}} = \Omega_{t_n}$, $\mathbf{u}^0_{n+1} = \mathbf{u}^h_n$ and $k = 0$
repeat
1. solve the mesh equation (39) for $\mathbf{w}^{k+1}_{n+1}$ in $\Omega_{t^k_{n+1}}$ using boundary conditions (37) and (38) with $\mathbf{u}^k_{n+1}$
2. update $\Omega_{t^{k+1}_{n+1}} = \Omega_{t^k_{n+1}} + \delta t \mathbf{w}^{k+1}_{n+1}$ using (36)
3. solve the FSI system (28) and (29) in $\Omega_{t^{k+1}_{n+1}}$ for $\mathbf{u}^{k+1}_{n+1}$ and p^{k+1}_{n+1}
4. $\epsilon_k = \frac{\|\mathbf{u}^{k+1}_{n+1} - \mathbf{u}^k_{n+1}\|}{\|\mathbf{u}^k_{n+1}\|}$, $k \leftarrow k+1$

until $\epsilon_k < tol$

Remark 3. The mesh equation (39) is discretised as a positive definite linear equation system, and we solve it efficiently using a preconditioned Conjugate Gradient (pCG) method (Nocedal, 1996). The FSI equations (28) and (29) are discretised as a saddle-point equation system. We use an operator splitting method and efficiently solve a convection and Stokes problem separately (Wang et al., 2017; Glowinski, 2003). We solve the convection equation using pCG and the Stokes equation using a preconditioned MinRes algorithm. The preconditioner for CG is an incomplete Cholesky decomposition of the system matrix, and the preconditioner of MinRes is an incomplete Cholesky decomposition of a modified system matrix, where the pressure mass matrix replaces the zero pressure block (Elman et al., 2014).

5. Stability analysis

We shall deduce an energy stability result for Problem 2 at the end of this section. In preparation for this we first prove the following lemmas.

Lemma 1. *If* $(\mathbf{u}, p, \mathbf{w})$ *is the solution of Problem 2, then* $\mathbf{u}$ *satisfies the following at* $t = t_{n+1}$.

$$\int_{\Omega_t} (\mathbf{u}\cdot\nabla)\,\mathbf{u}\cdot\mathbf{u} = 0. \tag{43}$$

Proof. Noticing that

$$\int_{\Omega_t} (\mathbf{u}\cdot\nabla)\,\mathbf{u}\cdot\mathbf{u} = \int_{\Omega_t} \nabla\cdot(\mathbf{u}\otimes\mathbf{u})\cdot\mathbf{u} - \int_{\Omega_t} |\mathbf{u}|^2\,\nabla\cdot\mathbf{u}, \tag{44}$$

and integrating by parts:

$$\begin{aligned} &\int_{\Omega_t} (\mathbf{u}\cdot\nabla)\,\mathbf{u}\cdot\mathbf{u} = \int_{\partial\Omega_t} |\mathbf{u}|^2\,\mathbf{u}\cdot\mathbf{n} - \int_{\Omega_t} (\mathbf{u}\cdot\nabla)\,\mathbf{u}\cdot\mathbf{u} - \int_{\Omega_t} |\mathbf{u}|^2\,\nabla\cdot\mathbf{u}. \\ &\Rightarrow \int_{\Omega_t} (\mathbf{u}\cdot\nabla)\,\mathbf{u}\cdot\mathbf{u} = \frac{1}{2}\int_{\partial\Omega_t} |\mathbf{u}|^2\,\mathbf{u}\cdot\mathbf{n} - \frac{1}{2}\int_{\Omega_t} |\mathbf{u}|^2\,\nabla\cdot\mathbf{u}. \end{aligned} \tag{45}$$

In the above $\int_{\partial\Omega_t} |\mathbf{u}|^2\,\mathbf{u}\cdot\mathbf{n} = 0$, thanks to the enclosed flow $\mathbf{u}\cdot\mathbf{n} = 0$ (17). Using the Sobolev imbedding theorem (Mitrovic and Zubrinic, 1997, Theorem 6 in Chapter 5), we have $H^1 \subset L^\infty$ in the two dimensional case and $H^1 \subset L^6$ in the three dimensional case. Either L^∞ or L^6 is included in L^4 because Ω_t has finite measure. Therefore $\mathbf{u} \in H^1 \subset L^4 \Rightarrow |\mathbf{u}|^2 \in L^2$, and $\int_{\Omega_t} |\mathbf{u}|^2\,\nabla\cdot\mathbf{u} = 0$ thanks to (29). □

Lemma 2. *If* $(\mathbf{u}, p, \mathbf{w})$ *is the solution of Problem 2 then, for any* $\mathbf{w} \in V^h(\Omega_t)$, $\mathbf{u}$ *satisfies the following at* $t = t_{n+1}$.

$$\xi(t) \equiv \int_{\Omega_t} (\mathbf{w}\otimes\mathbf{u}) : \nabla\mathbf{u} = -\frac{1}{2}\int_{\Omega_t} |\mathbf{u}|^2\,\nabla\cdot\mathbf{w}. \tag{46}$$

Proof. Integrating by parts we get

$$\xi(t) = \int_{\partial\Omega_t} (\mathbf{w}\otimes\mathbf{u})\,\mathbf{u}\cdot\mathbf{n} - \int_{\Omega_t} \nabla\cdot(\mathbf{w}\otimes\mathbf{u})\cdot\mathbf{u} \tag{47}$$

The boundary integral in (47) is zero due to the enclosed flow $\mathbf{u}\cdot\mathbf{n} = 0$ condition (17). The second term on the right-hand side of (47) can be expressed as:

$$\int_{\Omega_t} \nabla\cdot(\mathbf{w}\otimes\mathbf{u})\cdot\mathbf{u} = \xi(t) + \int_{\Omega_t} |\mathbf{u}|^2\,\nabla\cdot\mathbf{w}, \tag{48}$$

we then have (46) by substituting (48) into (47). □

Lemma 3. *If* $(\mathbf{u}_{n+1}, p_{n+1}, \mathbf{w}_{n+1})$ *is the solution of Problem 2, then*

$$\|\mathbf{u}_{n+1}\|^2_{0,\Omega_{t_{n+1}}} - \|\mathbf{u}_{n+1}\|^2_{0,\Omega_{t_n}} = \delta t \mathcal{I}(\eta), \tag{49}$$

with

$$\eta(t) = \int_{\Omega_t} |\mathbf{u}_{n+1}|^2 \nabla \cdot \mathbf{w}(t), \quad t \in (t_n, t_{n+1}). \tag{50}$$

Proof. Since

$$\begin{aligned} \eta(t) &= \int_{\Omega_{t_n}} J_{\mathcal{A}_{t_n,t}} |\mathbf{u}_{n+1}|^2 \left(\frac{\partial \mathcal{A}^{-1}_{t_n,t}}{\partial \mathbf{x}} \nabla_{\mathbf{x}_n} \right) \cdot \mathbf{w}(t) \\ &= \int_{\Omega_{t_n}} |\mathbf{u}_{n+1}|^2 \left(\mathbf{C}_{\mathcal{A}_{t_n,t}} \nabla_{\mathbf{x}_n} \right) \cdot \mathbf{w}(t), \end{aligned} \tag{51}$$

where $\mathbf{C}_{\mathcal{A}_{t_n,t}}$ is the cofactor matrix of $\frac{\partial \mathcal{A}_{t_n,t}}{\partial \mathbf{x}}$. According to the way we construct $\mathcal{A}_{t_n,t}$ (40), we know $\mathbf{C}_{\mathcal{A}_{t_n,t}}$ is a polynomial in time of degree $d-1$ (Nobile and Formaggia, 1999), with $d = 2, 3$ being the space dimension. Also $\mathbf{w}(t) = \mathbf{w}_{n+1}$ is a constant for $t \in (t_n, t_{n+1}]$, so $\eta(t)$ is linear in time when $d = 2$ and quadratic when $d = 3$, and a mid-point integration ($d = 2$) or Simpson formula ($d = 3$) would exactly compute $\int_{t_n}^{t_{n+1}} \eta(t)$. This is to say

$$\mathcal{I}(\eta) = \int_{t_n}^{t_{n+1}} \eta(t). \tag{52}$$

Noticing that for $t \in (t_n, t_{n+1})$,

$$\begin{aligned} \frac{d}{dt} \int_{\Omega_t} |\mathbf{u}_{n+1}|^2 &= \frac{d}{dt} \int_{\Omega_{t_n}} J_{\mathcal{A}_{t_n,t}} |\mathbf{u}_{n+1}|^2 \\ &= \int_{\Omega_{t_n}} J_{\mathcal{A}_{t_n,t}} |\mathbf{u}_{n+1}|^2 \nabla_{\mathbf{x}} \mathbf{w}(t) = \eta(t), \end{aligned} \tag{53}$$

and using (52), we finally have (49). □

Lemma 4. *Define potential energy of the solid:*

$$E(t) = \int_{\Omega^s_{t_0}} \Psi(\mathbf{F}). \tag{54}$$

If $(\mathbf{u}_{n+1}, p_{n+1}, \mathbf{w}_{n+1})$ *is the solution of Problem 2 and* $\Psi(\mathbf{F})$ *is* C^1 *convex on the set of second order tensors (Boffi and Gastaldi, 2016), then*

$$\delta t \int_{\Omega^s_{t_0}} \frac{\partial \Psi}{\partial \mathbf{F}} (\mathbf{F}_{n+1}) : \nabla_{\hat{\mathbf{x}}} \mathbf{u}_{n+1} \geq E(t_{n+1}) - E(t_n). \tag{55}$$

Proof. Let

$$w(t) = \Psi(\mathbf{F}_n + t(\mathbf{F}_{n+1} - \mathbf{F}_n)), \tag{56}$$

then

$$w'(t) = \frac{\partial \Psi}{\partial \mathbf{F}} (\mathbf{F}_n + t(\mathbf{F}_{n+1} - \mathbf{F}_n)) : (\mathbf{F}_{n+1} - \mathbf{F}_n). \tag{57}$$

Due to the convexity assumption of $\Psi(\mathbf{F})$, we have

$$w'(1) \geq w(1) - w(0). \tag{58}$$

This gives:

$$\frac{\partial \Psi}{\partial \mathbf{F}} (\mathbf{F}_{n+1}) : (\mathbf{F}_{n+1} - \mathbf{F}_n) \geq \Psi(\mathbf{F}_{n+1}) - \Psi(\mathbf{F}_n). \tag{59}$$

Using (35) we have

$$\delta t \frac{\partial \Psi}{\partial \mathbf{F}} (\mathbf{F}_{n+1}) : \nabla_{\hat{\mathbf{x}}} \mathbf{u}_{n+1} \geq \Psi(\mathbf{F}_{n+1}) - \Psi(\mathbf{F}_n). \tag{60}$$

which finally leads to (55) by integrating (60) in $\Omega^s_{t_0}$. □

Due to the arbitrariness of $\mathbf{v}$, q and $\mathbf{z}$, we now choose $\mathbf{v} = \mathbf{u}^h_{n+1}$, $q = -p^h_{n+1}$ and $\mathbf{z} = 0$ in Eq. (42) to deduce the stability result. Using Lemma 1, we have

$$\begin{aligned}
&\rho \int_{\Omega_{t_{n+1}}} \mathbf{u}^h_{n+1} \cdot \mathbf{u}^h_{n+1} - \rho \int_{\Omega_{t_n}} \mathbf{u}^h_n \cdot \mathbf{u}^h_{n+1} \\
&+ \delta t \rho \mathcal{I}\left(\xi(t)\right) + \frac{\delta t \mu^f}{2} \int_{\Omega^f_{t_{n+1}}} \mathrm{D}\mathbf{u}^h_{n+1} : \mathrm{D}\mathbf{u}^h_{n+1} \\
&+ \delta t \int_{\Omega^s_{t_0}} \frac{\partial \Psi}{\partial \mathbf{F}} \left(\mathbf{F}_{n+1}\right) : \nabla_{\hat{\mathbf{x}}} \mathbf{u}^h_{n+1} = \delta t \int_{\Omega_{t_{n+1}}} \rho \mathbf{g} \cdot \mathbf{u}^h_{n+1}.
\end{aligned} \tag{61}$$

Combining Lemmas 2 and 3 we have

$$\|\mathbf{u}_{n+1}\|^2_{0,\Omega_{t_n}} = \|\mathbf{u}_{n+1}\|^2_{0,\Omega_{t_{n+1}}} - \delta t \mathcal{I}\left(\eta\right) = \|\mathbf{u}_{n+1}\|^2_{0,\Omega_{t_{n+1}}} + \delta t \mathcal{I}\left(\xi\right). \tag{62}$$

Substituting Eq. (62) into the following estimate

$$\begin{aligned}
&\int_{\Omega_{t_n}} \mathbf{u}^h_n \cdot \mathbf{u}^h_{n+1} \leq \|\mathbf{u}^h_n\|_{0,\Omega_{t_n}} \|\mathbf{u}^h_{n+1}\|_{0,\Omega_{t_n}} \\
&\leq \frac{1}{2}\left(\|\mathbf{u}^h_n\|^2_{0,\Omega_{t_n}} + \|\mathbf{u}^h_{n+1}\|^2_{0,\Omega_{t_n}}\right),
\end{aligned} \tag{63}$$

we get

$$\int_{\Omega_{t_n}} \mathbf{u}^h_n \cdot \mathbf{u}^h_{n+1} \leq \frac{1}{2}\left(\|\mathbf{u}^h_n\|^2_{0,\Omega_{t_n}} + \|\mathbf{u}^h_{n+1}\|^2_{0,\Omega_{t_{n+1}}} + \delta t \mathcal{I}(\xi)\right). \tag{64}$$

Combining (61) and (64), and thanks to Lemma 4 the energy stability result reads:

Proposition 1 (*Energy Non-Increasing*). *Let* $\left(\mathbf{u}^h_{n+1}, p^h_{n+1}, \mathbf{w}^h_{n+1}\right)$ *be the solution of Problem 2, if there is no body force, then*

$$\begin{aligned}
&\frac{\rho}{2}\|\mathbf{u}^h_{n+1}\|^2_{0,\Omega_{t_{n+1}}} + E\left(t_{n+1}\right) + \frac{\delta t \mu^f}{2} \sum_{k=1}^{n+1} \int_{\Omega^f_{t_k}} \mathrm{D}\mathbf{u}^h_k : \mathrm{D}\mathbf{u}^h_k d\mathbf{x} \\
&\leq \frac{\rho}{2}\|\mathbf{u}^h_n\|^2_{0,\Omega_{t_n}} + E\left(t_n\right) + \frac{\delta t \mu^f}{2} \sum_{k=1}^{n} \int_{\Omega^f_{t_k}} \mathrm{D}\mathbf{u}^h_k : \mathrm{D}\mathbf{u}^h_k d\mathbf{x}.
\end{aligned} \tag{65}$$

The above estimate indicate that the total energy, including kinetic energy, potential energy and the viscous dissipation, of the FSI system is non-increasing.

Remark 4. The stability result (Proposition 1) is drawn under assumption of the homogeneous Dirichlet and Neumann boundary conditions (17), and without any body force. In this enclosed system, we prove that the interactions between fluids and solid in the FSI system is stable. Although the stability is only proved using an enclosed system, this also provides a strong indication of stability for other FSI systems if the input energy is stable.

6. Implementation: F -scheme and d-scheme

In this section, we focus on the implementation of a specific solid model, which determines the following term

$$\int_{\Omega^s_{t_0}} \frac{\partial \Psi}{\partial \mathbf{F}} \left(\mathbf{F}_{n+1}\right) : \nabla_{\hat{\mathbf{x}}} \mathbf{v} \tag{66}$$

in Eq. (42). We consider an incompressible neo-Hookean solid model with the energy function Ψ being given as follows (Hesch et al., 2014b):

$$\Psi\left(\mathbf{F}\right) = \frac{c_1}{2}\left[tr\left(\mathbf{F}\mathbf{F}^T\right) - d - 2ln\left(J_{\mathcal{F}_t}\right)\right]. \tag{67}$$

In order to compute the derivative of Ψ with respective to $\mathbf{F}$, we first have

$$\begin{aligned}
&\left[\frac{\partial tr\left(\mathbf{F}^T\mathbf{F}\right)}{\partial \mathbf{F}}\right]_{mn} = \frac{\partial tr\left(F_{ki}F_{kj}\right)}{\partial F_{mn}} = \frac{\partial \sum_k^d \sum_i^d F^2_{ki}}{\partial F_{mn}} \\
&= \frac{\partial\left(F^2_{11} + F^2_{12} + \cdots + F^2_{dd}\right)}{\partial F_{mn}} = 2\mathbf{F}_{mn}.
\end{aligned} \tag{68}$$

Let $cof(F_{ij}) = (-1)^{i+1} det$ ($\mathbf{F}$ without ith row and jth column) be the cofactor of F_{ij}. Because of $J_{\mathcal{F}_t} = \sum_k^d F_{ik} cof\ (F_{ik})$, we have $\frac{\partial J_{\mathcal{F}_t}}{\partial F_{ij}} = cof\ (F_{ij})$, i.e,

$$\frac{\partial J_{\mathcal{F}_t}}{\partial \mathbf{F}} = cof\ (\mathbf{F}) = J_{\mathcal{F}_t} \mathbf{F}^{-T}. \tag{69}$$

Combining Eqs. (68) and (69) gives

$$\frac{\partial \Psi}{\partial \mathbf{F}} = c_1 \left(\mathbf{F} - \mathbf{F}^{-T}\right). \tag{70}$$

Using formula (35), the term (66) can then be expressed as:

$$\begin{aligned} &\int_{\Omega^s_{t_0}} \frac{\partial \Psi}{\partial \mathbf{F}} (\mathbf{F}_{n+1}) : \nabla_{\hat{\mathbf{x}}} \mathbf{v} = c_1 \int_{\Omega^s_{t_0}} \left(\mathbf{F}_{n+1} - \mathbf{F}^{-T}_{n+1}\right) : \nabla_{\hat{\mathbf{x}}} \mathbf{v} \\ &= c_1 \int_{\Omega^s_{t_0}} \mathbf{F}_{n+1} : \nabla_{\hat{\mathbf{x}}} \mathbf{v} - c_1 \int_{\Omega^s_{t_{n+1}}} J^{-1}_{\mathcal{F}_t} \nabla \cdot \mathbf{v} \\ &= c_1 \delta t \int_{\Omega^s_{t_0}} \nabla_{\hat{\mathbf{x}}} \mathbf{u}_{n+1} : \nabla_{\hat{\mathbf{x}}} \mathbf{v} + c_1 \int_{\Omega^s_{t_0}} \mathbf{F}_n : \nabla_{\hat{\mathbf{x}}} \mathbf{v} - c_1 \int_{\Omega^s_{t_{n+1}}} J^{-1}_{\mathcal{F}_t} \nabla \cdot \mathbf{v}. \end{aligned} \tag{71}$$

In the above we update the solid deformation tensor $\mathbf{F}$ and integrate in the initial configuration, and we call this the $\mathbf{F}$-scheme. We can also express the stress in terms of displacement $\mathbf{d}$ and integrate in the current configuration as introduced in Hecht and Pironneau (2017), which is called the $\mathbf{d}$-scheme. To deduce the $\mathbf{d}$-scheme, we first transform the term (66) to be integrated in the current domain:

$$\int_{\Omega^s_{t_0}} \frac{\partial \Psi}{\partial \mathbf{F}} (\mathbf{F}_{n+1}) : \nabla_{\hat{\mathbf{x}}} \mathbf{v} = \int_{\Omega^s_{t_{n+1}}} J^{-1}_{\mathcal{F}_t} \frac{\partial \Psi}{\partial \mathbf{F}} \mathbf{F}^T : \nabla \mathbf{v} = \int_{\Omega^s_{t_{n+1}}} \boldsymbol{\tau}^s : \nabla \mathbf{v}, \tag{72}$$

where

$$\boldsymbol{\tau}^s = c_1 J^{-1}_{\mathcal{F}_t} (\mathbf{B} - \mathbf{I}) \tag{73}$$

is the deviatoric stress tensor, with $\mathbf{B} = \mathbf{F}\mathbf{F}^T$.

Let us only consider a two dimensional case, readers may refer to Chiang et al. (2017) for the three dimensional case. According to the Cayley–Hamilton theorem, $\mathbf{B}$ satisfies its characteristic equation:

$$\mathbf{B}^2 - tr_{\mathbf{B}} \mathbf{B} + J^2_{\mathcal{F}_t} \mathbf{I} = 0, \tag{74}$$

from which we immediately have:

$$\mathbf{B} = tr_{\mathbf{B}} \mathbf{I} - J^2_{\mathcal{F}_t} \mathbf{B}^{-1}. \tag{75}$$

Since

$$\mathbf{F} = \nabla_{\hat{\mathbf{x}}} \mathbf{x} = \nabla_{\hat{\mathbf{x}}} (\hat{\mathbf{x}} + \mathbf{d}) = \mathbf{I} + \mathbf{F} \nabla \mathbf{d}, \tag{76}$$

we also have:

$$\mathbf{F}^{-1} = \mathbf{I} - \nabla \mathbf{d}. \tag{77}$$

Substituting (75) and (77) into (73), $\boldsymbol{\tau}^s$ can be expressed by displacement as follows:

$$\boldsymbol{\tau}^s = -c_1 J_{\mathcal{F}_t} (\mathbf{I} - \nabla \mathbf{d})^T (\mathbf{I} - \nabla \mathbf{d}) + c_1 J^{-1}_{\mathcal{F}_t} (tr_{\mathbf{B}} - 1) \mathbf{I}, \tag{78}$$

which can further be written as

$$\boldsymbol{\tau}^s = c_1 J_{\mathcal{F}_t} \left(\mathrm{D}\mathbf{d} - \nabla^{\mathrm{T}} \mathbf{d} \nabla \mathbf{d}\right) + \bar{p} \mathbf{I}, \tag{79}$$

where $\bar{p} = c_1 J^{-1}_{\mathcal{F}_t} (tr_{\mathbf{B}} - 1) - c_1 J_{\mathcal{F}_t}$ will be integrated into the solid pressure p in (11) as an unknown. Similarly to the update of $\mathbf{F}$ in (35), updating the displacement by

$$\mathbf{d}_{n+1} = \tilde{\mathbf{d}}_n + \delta t \mathbf{u}_{n+1}, \quad \tilde{\mathbf{d}}_n = \mathbf{d}_n \circ \mathcal{A}^{-1}_{t_n, t_{n+1}}, \tag{80}$$

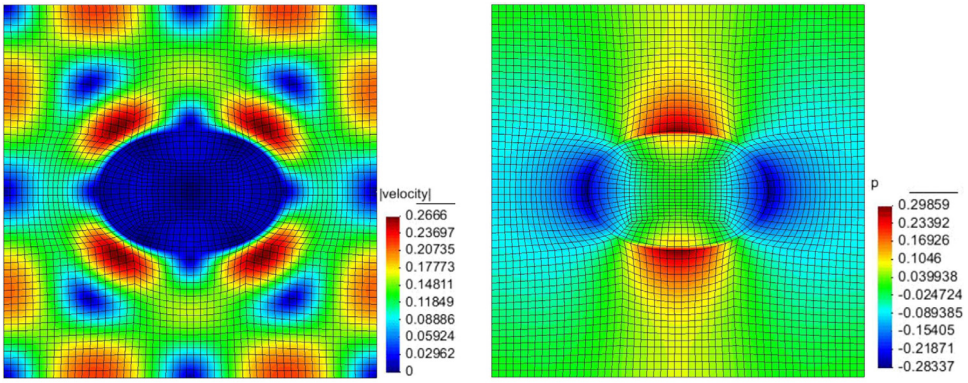

(a) Velocity norm. (b) Pressure.

Fig. 2. Snapshot of the oscillating disc at $t = 0.25$ when the disc is maximally stretched, using a time step of $\Delta t = 0.01$.

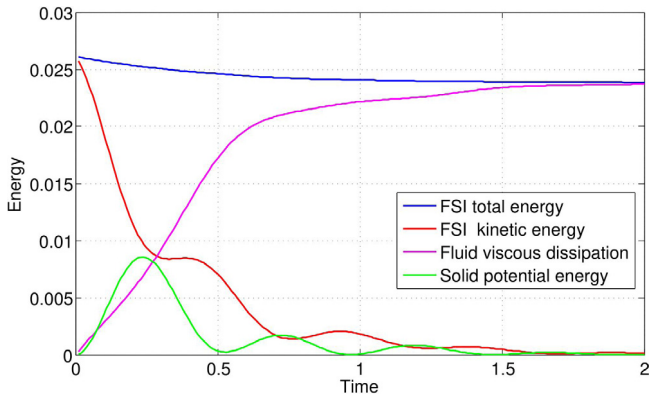

Fig. 3. Evolution of energy for the oscillating disc using $\Delta t = 0.01$. The peaks of the green curve indicate the time when the disc is maximally stretched. The first peak is horizontally stretched and the second peak is vertically stretched. The troughs of the green curve are the stress-free stages. (For interpretation of the references to colour in this figure legend, the reader is referred to the web version of this article.)

leads to the computation of term (66) as follows:

$$
\begin{aligned}
&\int_{\Omega^s_{t_0}} \frac{\partial \Psi}{\partial \mathbf{F}}\left(\mathbf{F}_{n+1}\right) : \nabla_{\hat{\mathbf{x}}}\mathbf{v} = \int_{\Omega^s_{t_{n+1}}} \boldsymbol{\tau}^s : \nabla \mathbf{v} \\
&= c_1 \int_{\Omega^s_{t_{n+1}}} \left(\mathrm{D}\mathbf{d}_{n+1} - \nabla^{\mathrm{T}}\mathbf{d}_{n+1}\nabla \mathbf{d}_{n+1}\right) : \nabla \mathbf{v} \\
&= \frac{c_1 \delta t}{2} \int_{\Omega^s_{t_{n+1}}} \mathrm{D}\mathbf{u}_{n+1} : \mathrm{D}\mathbf{v} + \frac{c_1}{2} \int_{\Omega^s_{t_{n+1}}} \mathrm{D}\tilde{\mathbf{d}}_n : \mathrm{D}\mathbf{v} \\
&- \delta t c_1 \int_{\Omega^s_{t_{n+1}}} \left(\nabla^{\mathrm{T}}\mathbf{u}_{n+1}\nabla \tilde{\mathbf{d}}_n + \nabla^{\mathrm{T}}\tilde{\mathbf{d}}_n \nabla \mathbf{u}_{n+1}\right) : \nabla \mathbf{v} \\
&- c_1 \int_{\Omega^s_{t_{n+1}}} \nabla^{\mathrm{T}}\tilde{\mathbf{d}}_n \nabla \tilde{\mathbf{d}}_n : \nabla \mathbf{v}.
\end{aligned}
\tag{81}
$$

Note that in the above, the second order term $O\left(\delta t^2\right)$ is neglected and $J_{\mathcal{F}_t}$ is replaced by 1. The stability of the **d**-scheme is proved in Hecht and Pironneau (2017) with the neglection of the term of order $O(\delta t^2)$, which may be regarded as a further approximation of the **F**-scheme.

Remark 5. The two and three dimensional **F**-scheme have exactly the same formulations. This can been seen from Eq. (71), which does not depend on dimensions. However the formulation of the **d**-scheme depends on the Cayley–Hamilton theorem, which is different in two and three dimensions, and consequently leads to significant complexity of the **d**-scheme

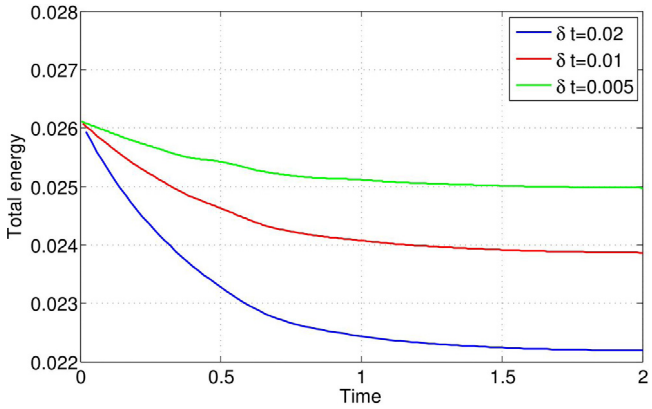

Fig. 4. Evolution of total energy for the oscillating disc.

in three dimensions (Chiang et al., 2017). It should be noted however that an advantage of the d-scheme is that, because it computes all integrals in the current domain, it is more straight forward to handle remeshing when it is required (Hecht and Pironneau, 2017).

Remark 6. Notice that Eq. (80) is a backward-Euler approximation for displacement **d** rather than velocity **u**. This choice is consistent with the overall first-order time discretisation. The mid-point rule is another choice, however the overall scheme is still first order, because the update of domain Ω_t is not straightforward to compute to second order (Pironneau, 2016a; Hecht and Pironneau, 2017).

7. Numerical experiments

In this section, we assess the reliability and stability of the proposed numerical scheme through a selection of benchmarks in the FSI area. We shall use the Taylor–Hood elements for the velocity–pressure pair. We validate the energy stability expressed by (65) in Section 7.1. We validate the proposed scheme against a FSI problem with a semi-analytic solution in Section 7.2. Time and mesh convergence tests are carried out in Section 7.3, and an example with very large solid deformation is tested in Section 7.4. The **F**-scheme will be adopted in all the following numerical tests. In addition, the **d**-scheme is also implemented for tests in Sections 7.1 and 7.4 in order to compare the two schemes.

We use the following consistent units for all the numerical tests in this section: length (m), time (s) , velocity (m/s), acceleration (m/s^2), mass (kg), force (N), pressure/stress (N/m^2), density (kg/m^3) and viscosity (N $\cdot$ s/m^2).

7.1. Oscillating disc

In this test, we consider an enclosed flow ($\mathbf{n}\cdot\mathbf{u}=0$) in $\Omega=[0,1]\times[0,1]$ with a periodic boundary condition. A solid disc is initially located in the middle of the square Ω and has a radius of 0.2. The initial velocity of the fluid and solid are prescribed by the following stream function

$$\Psi = \Psi_0 \sin(ax)\sin(by),$$

where $\Psi_0 = 5.0\times10^{-2}$ and $a=b=2\pi$. In this test, $\rho^f=1$, $\mu^f=0.01$, $\rho^s=1.5$ and $c_1=1$. Taking the maximum initial velocity $2\pi\Psi_0=\hat{U}$ and the height of domain Ω, $\hat{H}=1$, as the characteristic velocity and length respectively, the Reynolds number is: $Re=\frac{\rho^f\hat{U}\hat{H}}{\mu^f}=10\pi$. A mesh size of 3217 elements with 13081 nodes is used in this test. In order to visualise the flow a snapshot ($t=0.25$) of the velocity and pressure field are presented in Fig. 2, and the evolution of energy is presented in Figs. 3 and 4 from which we can observe the property of non-increasing total energy as proved in Proposition 1.

The **F**-scheme and **d**-scheme are compared using this example and we have not found any significant difference by comparing the solid deformation as shown in Fig. 5.

7.2. Rotating disc

This test is taken from Hecht and Pironneau (2017). The computational domain is the area between two concentric circles (R_0 and R_1) as shown in Fig. 6, with fluid and solid properties as $\rho^f=1$, $\rho^s=2$, $\mu^f=2$ and $c_1=4$. A constant angular velocity ($\omega=U/R_1=0.6$) is prescribed at the outer boundary and the velocity on the inner boundary is set to be zero. Taking the value of velocity U and length R_1 as references, the Reynolds number is: $Re=\frac{\rho^f U R_1}{\mu^f}=7.5$. This

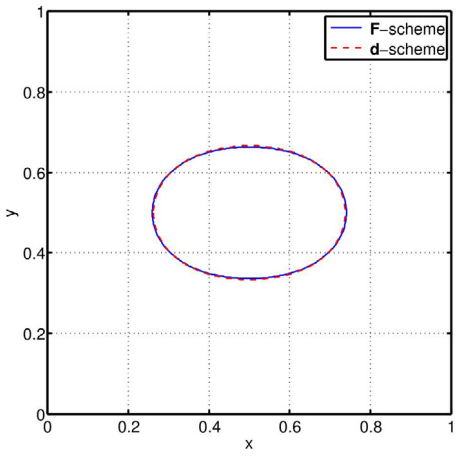

Fig. 5. Comparison of disc shape for the **F**-scheme and **d**-scheme at $t = 0.25$ when the disc is maximally stretched.

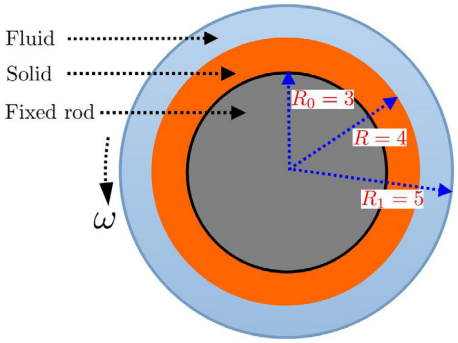

Fig. 6. Sketch of a rotating disc in Section 7.2.

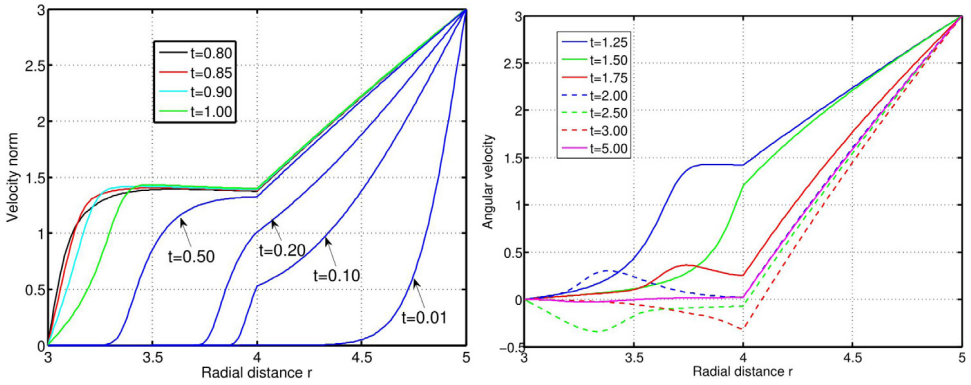

Fig. 7. Evolution of the velocity norm for the reduced one-dimensional rotating disc.

velocity first induces the fluid, that is initially at rest, to rotate and then gradually drags the solid to rotate as well. For a long-term run, the solid disc will oscillate, and its velocity will finally be damped to 0 as shown in Fig. 7. However, in this paper we are interested in time t = 0.85 when the solid has its largest deformation. Using the property of symmetry, this problem can be reduced to a one-dimensional equation when considered in a polar coordinate system (r, θ) (Hecht and Pironneau, 2017):

$$\rho^f \frac{\partial u_\theta}{\partial t} = \frac{\mu^f}{r}\frac{\partial}{\partial r}\left(r\frac{\partial u_\theta}{\partial r}\right) - \mu^f \frac{u_\theta}{r^2}, \qquad R \le r < R_1 \tag{82}$$

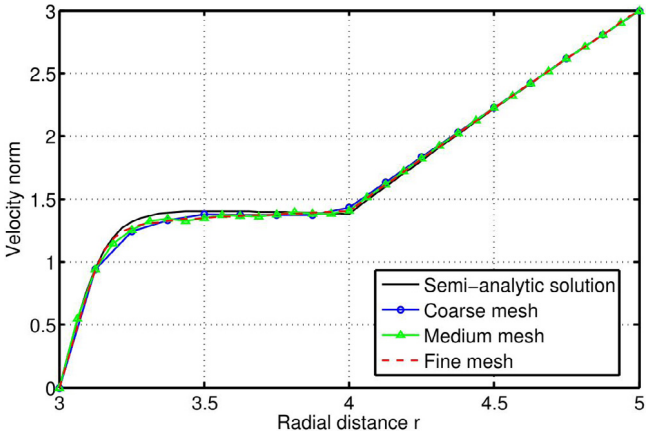

Fig. 8. Comparison between the proposed approach and the semi-analytic solution at $t = 0.85$ when the solid is maximally deformed.

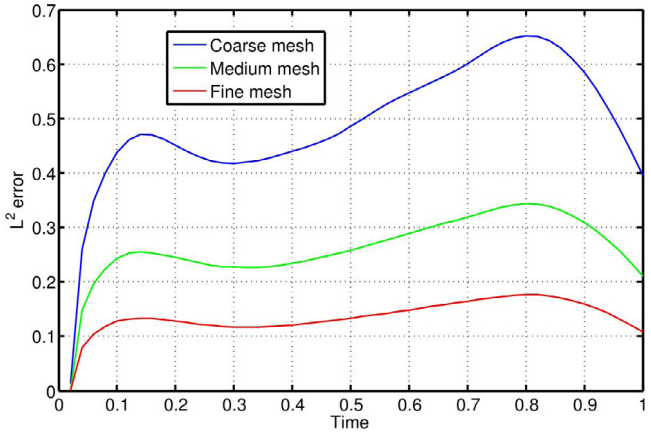

Fig. 9. Convergence of L^2 error.

and

$$\rho^s \frac{\partial u_\theta}{\partial t} = \frac{c_1}{r}\frac{\partial}{\partial r}\left(r\frac{\partial d_\theta}{\partial r}\right) - c_1\frac{d_\theta}{r^2}, \quad \frac{\partial d_\theta}{\partial t} = u_\theta, \qquad R_0 < r \le R, \tag{83}$$

where u_r and u_θ are the velocity components in the radial and tangential directions respectively. This one-dimensional problem (82) and (83) can be solved numerically to high accuracy, and the solution is plotted in Fig. 7 using 200 linear elements and $\Delta t = 1.0 \times 10^{-3}$. Using the same time step, which is stable, the proposed method can produce results of similar accuracy to the semi-analytic solution (i.e. the high-accuracy numerical solution of (82) and (83)), as shown in Fig. 8. We use three different meshes to test convergence of the proposed algorithm. A coarse mesh equally divides the radial direction of the computational domain into 4 segments, and equally divides the tangential direction into to 40 segments, which therefore has $4 \times 40 = 160$ biquadratic elements. The medium and fine meshes are refined based on the coarse mesh, which have $8 \times 80 = 640$ and $16 \times 160 = 2560$ elements respectively. Due to the discontinuity in the derivative at the fluid–solid interface, we only achieve an $O(h)$ convergence as shown in Fig. 9, where h is the mesh size. This observation is consistent with the result in Hecht and Pironneau (2017).

7.3. Oscillating flag

In this section, we consider an oscillating flag attached to a cylinder, which was firstly proposed in Turek and Hron (2006) (named FSI3), and been regarded as a challenging numerical test in the FSI field. We test the time and mesh convergence for the proposed FSI method. The computational domain is a rectangle $(L \times H)$ with a cut hole of radius r and centre (c, c) as shown in Fig. 10. A leaflet of size $l \times h$ is attached to the boundary of the hole (the mesh of the leaflet is fitted to the boundary of the hole, see the solid mesh in Fig. 11). In this test, $L = 2.5$, $H = 0.41$, $l = 0.35$, $h = 0.02$, $c = 0.2$ and $r = 0.05$. The fluid and solid parameters are as follows: $\rho^f = \rho^s = 10^3$, $\mu^f = 1$ and $c_1 = 2.0 \times 10^6$. Taking

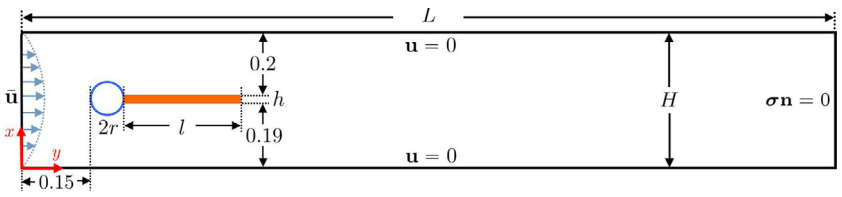

Fig. 10. Computational domain and boundary conditions for the oscillating flag.

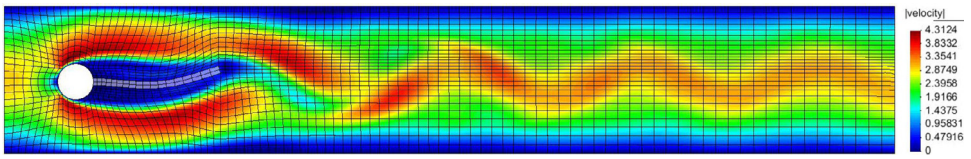

Fig. 11. A snap shot of the velocity norms at$t = 6$ using a coarse mesh.

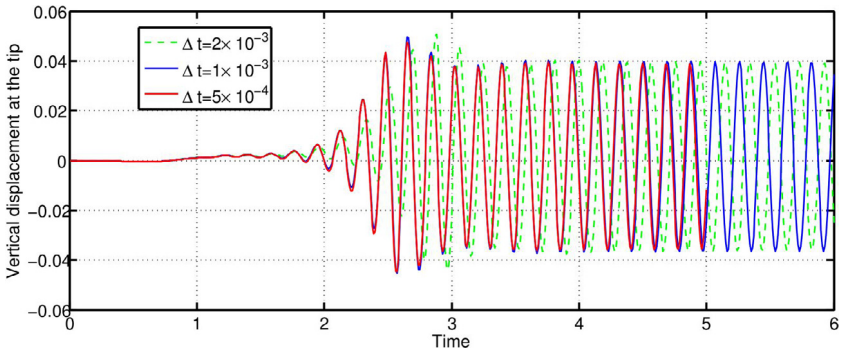

Fig. 12. Vertical displacement at the flag tip as a function of time, using different time step and a medium mesh (data of the red curve is plotted up to $t = 5$ for a better visualisation of the blue curve). (For interpretation of the references to colour in this figure legend, the reader is referred to the web version of this article.)

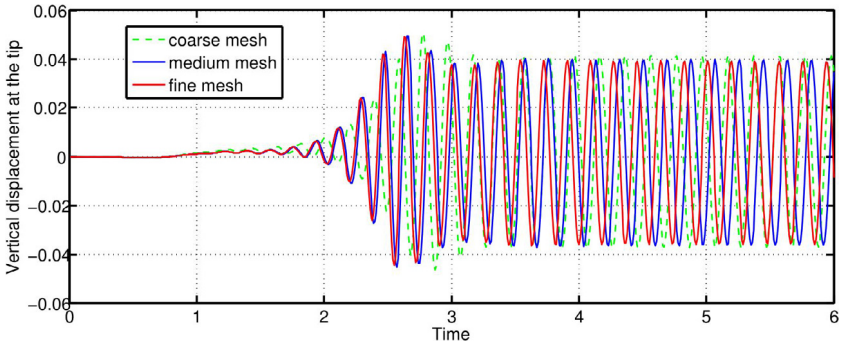

Fig. 13. Vertical displacement at the flag tip as a function of time, using different mesh size and a time step size of $\Delta t = 5 \times 10^{-4}$.

$\bar{U} = \int_0^H \bar{u}_x dy = 2H$ and the channel height H as the characteristic velocity and length respectively, the Reynolds number is: $Re = \frac{\rho^f \bar{U} H}{\mu^f} = 336.2$. The inlet flow is prescribed as:

$$\bar{u}_x = \frac{12y}{H^2}(H - y), \quad \bar{u}_y = 0. \tag{84}$$

A wall boundary condition and the outlet flow condition are displayed in Fig. 10. A coarse mesh has 10054 nodes and 2448 biquadratic elements as shown in Fig. 11, and a medium and fine mesh have 33746 nodes (8320 elements) and 68974 nodes (17081 elements) respectively. We study the oscillating frequency and amplitude at the tip of the flag. The convergence with respect to time and space are displayed in Figs. 12 and 13 respectively, and the period and

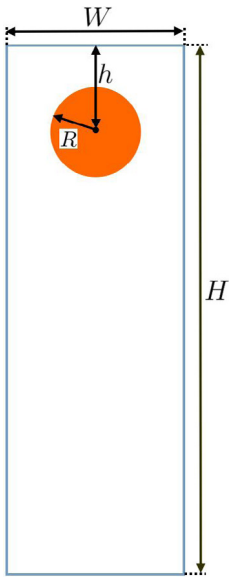

Fig. 14. Sketch of the falling disc.

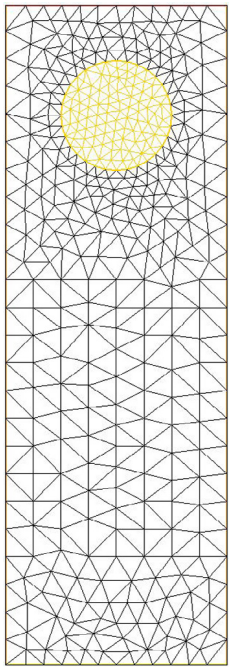

Fig. 15. Initial mesh for the falling disc.

amplitude of the oscillation converge to 5.26×10^{-3} and 0.0018 ± 0.0365 respectively. These figures have a good agreement with the reference values given in Turek and Hron (2006) with oscillation period and amplitude being 5.3×10^{-3} and 0.00148 ± 0.03438 respectively.

7.4. Falling disc

In this test, we simulate a falling disc due to gravity (Zhang and Gay, 2007; Hesch et al., 2014b), which needs remeshing in order to guarantee the mesh quality. However we will demonstrate that one needs much less remeshing, using the

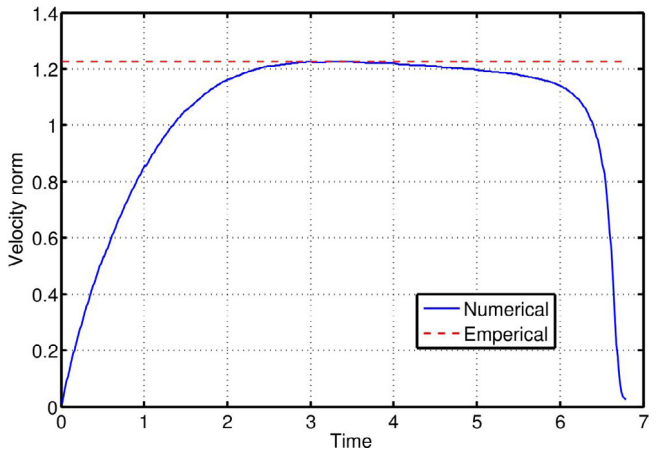

Fig. 16. Comparison between the numerical and empirical velocity of the falling disc.

proposed ALE methods, compared to methods using pure remesh in order to fit the fluid–solid interface (Hecht and Pironneau, 2017). This test is implemented using FreeFEM++ (Hecht, 2012).

The computational domain is a vertical channel with a disc placed at the top of the channel as illustrated in Fig. 14, where $W = 4$, $H = 12$, $h = 2$ and $R = 1$. In this test, $\rho^f = 1$, $\rho^s = 1.5$ $\mu^f = 0.1$, $c_1 = 10^4$ and the gravity acceleration is $g = -9.81$. The fluid velocity is fixed to be 0 on all boundaries except the top, which uses the zero-normal-stress boundary condition, i.e. $\boldsymbol{\sigma}\mathbf{n} = \mathbf{0}$. Notice that we choose c_1 sufficiently large so that the solid behaves as a rigid body. The computational domain is initially discretised by using 820 P_2/P_1 triangles with 1713 nodes as shown in Fig. 15. We use a stable time step size of $\delta t = 0.01$ and remesh every 100 times. We compare the simulation result against the empirical solution of a rigid ball falling in a viscous fluid (Hesch et al., 2014a), for which the maximal velocity U_m under gravity is given by

$$U_m = \frac{\left(\rho^s - \rho^f\right) g R^2}{4\mu^f}\left[\ln\left(\frac{W}{2R}\right) - 0.9157 + 1.7244\left(\frac{2R}{W}\right)^2 - 1.7302\left(\frac{2R}{W}\right)^4\right].$$

In the test $U_m = 1.2263$. Taking this final velocity U_m and the disc radius R as the characteristic velocity and length respectively, the Reynolds number is: $Re = \frac{\rho^f U_m R}{\mu^f} = 12.263$. The numerical and the empirical solutions agree well with each other when disc becomes stable as shown in Fig. 16. It can be understood that the disc velocity gradually decreases when it is close to the bottom of the channel. The evolution of the disc is displayed in Fig. 17. If we move the mesh by fluid velocity without the proposed ALE techniques, and remesh to guarantee the mesh quality then, for this example, we find that remeshing has to be taken at least every 7 time steps, otherwise the disc cannot successfully arrive at the bottom of the channel. We have also compared the **F**-scheme and **d**-scheme using this numerical test, and found that they presented very similar results (hence the latter are not shown in the figures here).

8. Conclusion

In this paper, we develop the one-field finite element method for Fluid–Structure Interaction (FSI), which only solves one-velocity field in the whole domain. We formulate the FSI system in an Arbitrary Lagrangian–Eulerian (ALE) coordinate system, solve it in a fully-coupled manner, and prove this ALE-FSI formulation is unconditionally stable by analysing the total energy of the whole system. The stability result is achieved by expressing the problem in a conservative form, and adopting an exact quadrature rule in order to eliminate the mesh velocity. Several numerical tests are presented in order to validate the proposed scheme, including testing the energy stability, validating against a semi-analytical solution and a benchmark case, and combining with a remeshing technique to simulate the case of extremely large solid displacement.

The stability proofs given in this manuscript are restricted to the case where the backward Euler scheme is applied in time. We expect the forward Euler scheme to be conditionally stable but potentially with much more restrictive time-step size than in the implicit case. We have not analysed the use of other implicit time-discretisation schemes, such as BDF2 or Crank–Nicolson, since these add significant complexity to the problem. In particular, as with all ALE schemes, the stability depends critically on the unknown mesh velocities, which makes the analysis very challenging in these higher order cases.

We test a variety of numerical examples, including a strong non-linear FSI problem such as the oscillating flag in test 7.3, which is regarded as a challenging benchmark in the FSI field, In none of the test cases that we have considered have we observed any instabilities.

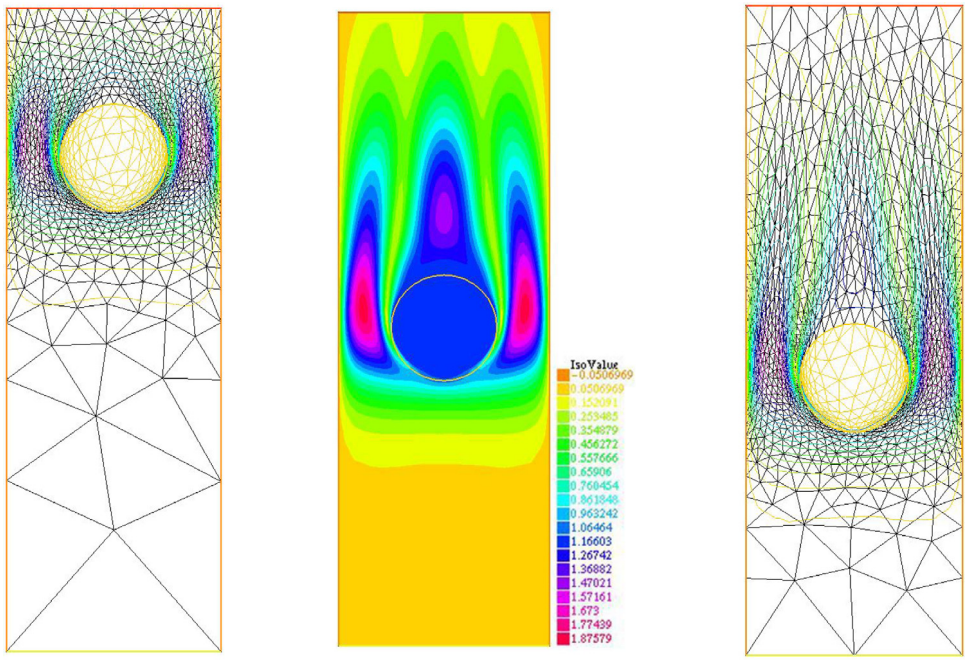

(a) $t = 2.0$. (b) $t = 3.5$. (c) $t = 4.0$.

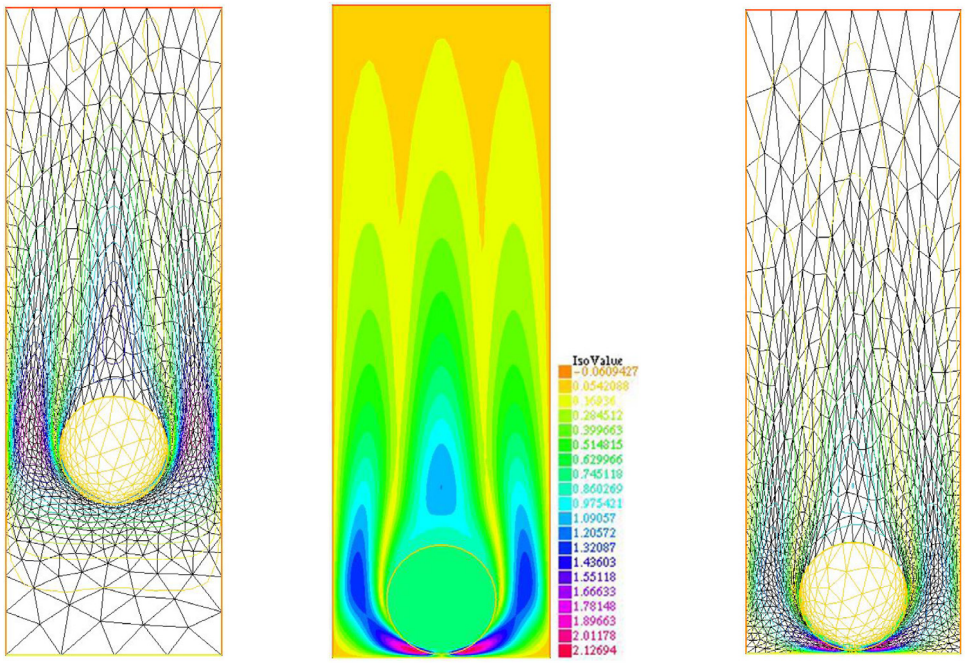

(d) $t = 5.5$. (d) $t = 6.0$. (d) $t = 6.8$.

Fig. 17. Evolution of the falling disc, with colour showing the velocity norm. (For interpretation of the references to colour in this figure legend, the reader is referred to the web version of this article.)

CRediT authorship contribution statement

Yongxing Wang: Conceptualization, Methodology, Software, Validation, Formal analysis, Investigation, Writing - original draft, Visualization. **Peter K. Jimack:** Supervision, Data curation, Writing - original draft, Writing - review &

editing, Project administration. **Mark A. Walkley:** Funding acquisition, Supervision, Writing - review & editing, Project administration. **Olivier Pironneau:** Supervision, Writing - review & editing, Validation, Resources.

Declaration of competing interest

The authors declare that they have no known competing financial interests or personal relationships that could have appeared to influence the work reported in this paper.

References

Belytschko, T., Liu, W.K., Moran, B., Elkhodary, K., 2013. Nonlinear Finite Elements for Continua and Structures. John Wiley & Sons.

Bendiksen, O., 1991. A new approach to computational aeroelasti. In: 32nd Structures, Structural Dynamics, and Materials Conference. pp. 939.

Bendiksen, K.H., Maines, D., Moe, R., Nuland, S., et al., 1991. The dynamic two-fluid model OLGA: Theory and application. SPE Prod. Eng. 6 (02), 171–180.

Blom, F.J., 1998. A monolithical fluid-structure interaction algorithm applied to the piston problem. Comput. Methods Appl. Mech. Engrg. 167 (3–4), 369–391.

Boffi, D., Cavallini, N., Gastaldi, L., 2015. The finite element immersed boundary method with distributed Lagrange multiplier. SIAM J. Numer. Anal. 53 (6), 2584–2604. http://dx.doi.org/10.1137/140978399.

Boffi, D., Gastaldi, L., 2016. A fictitious domain approach with Lagrange multiplier for fluid-structure interactions. Numer. Math. 135 (3), 711–732. http://dx.doi.org/10.1007/s00211-016-0814-1.

Bonito, A., Kyza, I., Nochetto, R.H., 2013. Time-discrete higher-order ALE formulations: stability. SIAM J. Numer. Anal. 51 (1), 577–604.

Brenner, S., Scott, R., 2007. The Mathematical Theory of Finite Element Methods, Vol. 15. Springer Science & Business Media.

Chiang, C.-Y., Pironneau, O., Sheu, T., Thiriet, M., 2017. Numerical study of a 3D Eulerian monolithic formulation for incompressible fluid-structures systems. Fluids 2 (2), 34.

Du, Q., Gunzburger, M.D., Hou, L.S., Lee, J., 2003. Analysis of a linear fluid-structure interaction problem. Discrete Contin. Dyn. Syst. 9 (3), 633–650.

Elman, H.C., Silvester, D.J., Wathen, A.J., 2014. Finite Elements and Fast Iterative Solvers: With Applications in Incompressible Fluid Dynamics. Oxford University Press, USA.

Formaggia, L., Nobile, F., 2004. Stability analysis of second-order time accurate schemes for ALE–FEM. Comput. Methods Appl. Mech. Engrg. 193 (39–41), 4097–4116.

Glowinski, R., 2003. Finite element methods for incompressible viscous flow. Handb. Numer. Anal. 9, 3–1176.

Grandmont, C., Maday, Y., 2000. Existence for an unsteady fluid-structure interaction problem. ESAIM Math. Model. Numer. Anal. 34 (3), 609–636.

Hecht, F., 2012. New development in FreeFem++. J. Numer. Math. 20 (3–4), 251–265, https://freefem.org/.

Hecht, F., Pironneau, O., 2017. An energy stable monolithic Eulerian fluid-structure finite element method. Internat. J. Numer. Methods Fluids 85 (7), 430–446. http://dx.doi.org/10.1002/fld.4388.

Heil, M., 2004. An efficient solver for the fully coupled solution of large-displacement fluid–structure interaction problems. Comput. Methods Appl. Mech. Engrg. 193 (1–2), 1–23. http://dx.doi.org/10.1016/j.cma.2003.09.006.

Heil, M., Hazel, A.L., Boyle, J., 2008. Solvers for large-displacement fluid–structure interaction problems: segregated versus monolithic approaches. Comput. Mech. 43 (1), 91–101. http://dx.doi.org/10.1007/s00466-008-0270-6.

Hesch, C., Gil, A., Carreno, A.A., Bonet, J., Betsch, P., 2014a. A mortar approach for fluid–structure interaction problems: Immersed strategies for deformable and rigid bodies. Comput. Methods Appl. Mech. Engrg. 278, 853–882.

Hesch, C., Gil, A.J., Carreño, A.A., Bonet, J., Betsch, P., 2014b. A mortar approach for fluid–structure interaction problems: Immersed strategies for deformable and rigid bodies. Comput. Methods Appl. Mech. Engrg. 278, 853–882. http://dx.doi.org/10.1016/j.cma.2014.06.004.

Hübner, B., Walhorn, E., Dinkler, D., 2004. A monolithic approach to fluid–structure interaction using space–time finite elements. Comput. Methods Appl. Mech. Engrg. 193 (23–26), 2087–2104.

Lequeurre, J., 2011. Existence of strong solutions to a fluid-structure system. SIAM J. Math. Anal. 43 (1), 389–410.

Magnus, J.R., Neudecker, H., 2019. Matrix Differential Calculus with Applications in Statistics and Econometrics. John Wiley & Sons.

Mitrovic, D., Zubrinic, D., 1997. Fundamentals of Applied Functional Analysis, Vol. 91. CRC Press.

Muddle, R.L., Mihajlović, M., Heil, M., 2012. An efficient preconditioner for monolithically-coupled large-displacement fluid–structure interaction problems with pseudo-solid mesh updates. J. Comput. Phys. 231 (21), 7315–7334. http://dx.doi.org/10.1016/j.jcp.2012.07.001.

Nobile, F., Formaggia, L., 1999. A stability analysis for the arbitrary Lagrangian Eulerian formulation with finite elements. East-West J. Numer. Math. 7 (ARTICLE), 105–132.

Nobile, F., Vergara, C., 2008. An effective fluid-structure interaction formulation for vascular dynamics by generalized Robin conditions. SIAM J. Sci. Comput. 30 (2), 731–763.

Nocedal, J., 1996. Conjugate gradient methods and nonlinear optimization. In: Linear and Nonlinear Conjugate Gradient-Related Methods. SIAM, Philadelphia, pp. 9–23.

Pironneau, O., 2016a. Numerical study of a monolithic fluid–structure formulation. In: Variational Analysis and Aerospace Engineering. Springer, pp. 401–420.

Pironneau, O., 2016b. Numerical study of a monolithic fluid–structure formulation. In: Variational Analysis and Aerospace Engineering. Springer International Publishing, pp. 401–420. http://dx.doi.org/10.1007/978-3-319-45680-5_15.

Richter, T., Wick, T., 2010. Finite elements for fluid–structure interaction in ALE and fully Eulerian coordinates. Comput. Methods Appl. Mech. Engrg. 199 (41–44), 2633–2642.

Turek, S., Hron, J., 2006. Proposal for numerical benchmarking of fluid–structure interaction between an elastic object and laminar incompressible flow. In: Fluid-Structure Interaction. Springer, pp. 371–385.

Wang, Y., Jimack, P.K., Walkley, M.A., 2017. A one-field monolithic fictitious domain method for fluid–structure interactions. Comput. Methods Appl. Mech. Engrg. 317, 1146–1168. http://dx.doi.org/10.1016/j.cma.2017.01.023.

Wang, Y., Jimack, P.K., Walkley, M.A., 2019. Energy analysis for the one-field fictitious domain method for fluid-structure interactions. Appl. Numer. Math. 140, 165–182. http://dx.doi.org/10.1016/j.apnum.2019.02.003.

Zhang, L.T., Gay, M., 2007. Immersed finite element method for fluid-structure interactions. J. Fluids Struct. 23 (6), 839–857. http://dx.doi.org/10.1016/j.jfluidstructs.2007.01.001.